

Breaking Rossby waves drive extreme precipitation in the world's arid regions

Authors: Andries Jan de Vries^{1,2}, Moshe Armon², Klaus Klingmüller³, Raphael Portmann^{2,4}, Matthias Röthlisberger², Daniela I.V. Domeisen^{1,2}

Author affiliations

¹Institute of Earth Surface Dynamics, University of Lausanne, Lausanne, Switzerland

²Institute for Atmospheric and Climate Science, ETH Zürich, Zürich, Switzerland

³Atmospheric Chemistry, Max Planck Institute for Chemistry, Mainz, Germany

⁴Climate and Agriculture, Agroscope Reckenholz, Zürich, Switzerland

Abstract

More than a third of the world's population lives in drylands and is disproportionately at risk of hydrometeorological hazards such as drought and flooding. While existing studies have widely explored weather systems governing precipitation formation in humid regions, our understanding of the atmospheric processes generating precipitation in arid regions remains fragmented at best. Here we show, using a variety of precipitation datasets, that Rossby wave breaking is a key atmospheric driver of precipitation in arid regions worldwide. Rossby wave breaking contributes up to 90% of daily precipitation extremes and up to 80% of total precipitation amounts in arid regions equatorward and downstream of the midlatitude storm tracks. The relevance of Rossby wave breaking for precipitation increases with increasing land aridity. Contributions of wave breaking to precipitation dominate in the poleward and westward portions of arid subtropical regions during the cool season. Given the projected precipitation decline and the large uncertainty in projections of precipitation extremes in these regions, our findings imply that Rossby wave breaking plays a crucial role in projections and uncertainties of future precipitation changes in societally vulnerable regions that are exposed to both freshwater shortages and flood hazards.

Keywords: rainfall, drylands, atmospheric dynamics, Rossby wave breaking, floods, climate change, freshwater resources.

Introduction

Drylands cover more than 40% of the Earth's land surface and host more than two billion people. These dry regions are projected to expand in a warming climate¹ along with an expected doubling of the number of people living in these regions by the end of the 21st century². The population in these

regions is disproportionally exposed to hydrometeorological hazards such as flooding³ and drought (Tanarhte, Chfadi, A.J. de Vries & Zittis, accepted in *Earth-Science Reviews*) as developing countries, which are common in these regions, often have limited resources to mitigate flood hazards and freshwater shortages⁴. A horrific example is the destructive flooding that unfolded in Libya in September 2023 and left at least 4,000 people dead and another 10,000 missing (<https://www.bbc.com/news/world-africa-66961312>). On the other hand, precipitation in arid regions replenishes scarce freshwater resources on which food security and ecosystems rely^{5,6}. Precipitation deficits and severe droughts in already water-scarce regions, amplified by climate change, have been suggested to foster armed conflict^{7,8} and migration⁹. Further increased stress on water resources in the future will likely put societies that are already affected by political and economic instability, civil unrest, and armed conflict under even larger pressure.

Climate models generally project a decline in precipitation amounts in much of the dry subtropics^{10,11}, while the intensities of the most severe precipitation extremes are anticipated to increase¹²⁻¹⁵, exacerbating the dual impacts of precipitation in these regions under global warming. However, projected changes in precipitation in these regions are subject to large uncertainties that stem from the atmospheric circulation that features a spatially varying response to climate change and is affected by internal climate variability and model bias¹⁶. Whereas atmospheric thermodynamics leads to spatially homogenous and robust increases in extreme precipitation intensities globally, atmospheric dynamics can modify the extreme precipitation response to global warming at a regional level, particularly in the dry subtropics¹⁷. Understanding the atmospheric dynamics that govern precipitation formation in these dry regions is thus a prerequisite for developing plausible storylines of hydrometeorological hazards in arid regions in a future climate as well as for a process-based climate model evaluation regarding these hazards.

Weather systems at synoptic scales (~1,000 km and one to several days) that govern precipitation formation in humid tropical and extratropical regions have been widely studied from a global perspective. In humid extratropical regions, precipitation largely results from extratropical cyclones^{18,19} and associated warm conveyor belts²⁰, fronts^{21,22}, and atmospheric rivers^{23,24}. In humid (sub)tropical regions, precipitation is often associated with tropical cyclones²⁵, monsoon lows²⁶, and tropical easterly waves²⁷. However, synoptic-scale weather systems governing precipitation in arid regions have virtually only been studied at the regional scale, pointing to a variety of atmospheric processes at play²⁸⁻³⁴. These processes often include upper-level troughs^{35,36} and cutoff lows³⁷⁻⁴⁰ of

midlatitude origin, suggesting a key role of extratropical wave breaking into low latitudes for the formation of precipitation in arid regions.

Atmospheric Rossby waves owe their existence to the rotation and spherical shape of the Earth⁴¹ and are of central importance for midlatitude weather and extreme events^{42,43}. Rossby waves can amplify and overturn in the meridional direction, leading to the breaking of these waves and vigorous mixing of air masses between higher and lower latitudes^{44,45}. Rossby wave breaking (RWB) can support the formation of precipitation by providing both atmospheric moisture advection and forcing for ascent, making the atmosphere conducive to deep moist convection^{46,47}. Existing studies have linked RWB to observed precipitation extremes in several regions, including North America⁴⁸, the Alpine region⁴⁹, and the Middle East⁵⁰ as well as to reanalysis-based precipitation in subtropical and extratropical regions globally^{51,52}.

Here, we quantify the contribution of RWB to both *precipitation extremes* and *total amounts* in arid regions worldwide using a variety of precipitation datasets. We identify RWB by combining diagnostics for potential vorticity streamers and cutoffs (see Methods) and applying these diagnostics to atmospheric reanalysis data. Given that precipitation is a challenging variable to measure, we quantify the contribution of wave breaking to precipitation using precipitation data from reanalysis, satellite-based estimates, station-based observations, and a product that combines these three different data sources (see Methods).

Results

Contribution of RWB to precipitation globally

We demonstrate the importance of RWB as a driver of precipitation in arid regions by 8 catastrophic flood events that caused fatalities and damage in different arid regions around the world (Extended Data Fig. 1 and Extended Data Table 1). To quantify the portion of precipitation that forms under the influence of RWB, we compute the fractions of *daily extreme precipitation occurrences* and *precipitation amounts* that coincide with RWB in a climatological year-round analysis and examine where this relation has a significant positive association (see Methods). RWB significantly contributes to precipitation in subtropical and extratropical regions equatorward and downstream of the midlatitude storm tracks (Fig. 1), where wave breaking occurs relatively frequently compared to other regions (Extended Data Fig. 2). Fractions of daily precipitation extremes attributed to RWB exceed 80-90% in southwest and central North America, the entire Mediterranean Basin and adjacent parts of North Africa, the Middle East and eastern Europe, the Atacama region, Patagonia, and the southern

flanks of southern Africa and Australia (Fig. 1a). In the same regions, up to 70-80% of the total annual precipitation amounts are significantly associated with RWB (Fig. 1b). Evaluation of all four precipitation datasets provides generally consistent estimates of precipitation patterns and fractions associated with RWB (Fig. 1 and Extended Data Fig. 3).

In contrast to the aforementioned regions, RWB has a significant negative association with precipitation in humid low- and high-latitude regions where other weather systems are primarily responsible for precipitation formation (Fig. 1 and Extended Data Fig. 3). Prominent regions emerge over the eastern parts of the North American and Asian continents and adjacent western parts of the North Pacific and North Atlantic Ocean basins, where tropical cyclones²⁵, extratropical cyclones^{18,19}, and fronts^{21,22} govern much of the precipitation formation. Other regions where precipitation has a significant negative association with RWB can be found over the extratropical west coasts of North America, Europe, southern South America, and New Zealand, where landfalling atmospheric rivers dominate precipitation generation^{23,24}.

The relevance of RWB for precipitation follows the seasonality of the large-scale circulation (Fig. 2 and Extended Data Figs. 4-7). In winter, fractions of precipitation significantly associated with RWB reach largest values over lower latitudes when the midlatitude storm tracks attain their strongest intensity and most equatorward influence⁵³. For example, hotspots of winter precipitation attributed to wave breaking emerge over southwestern North America and the Mediterranean in the Northern Hemisphere (Fig. 2a,c) and the Atacama region, southern Africa, and southern Australia in the Southern Hemisphere (Fig. 2b,d). In summer, large fractions of precipitation significantly associated with wave breaking are evident at higher latitudes over central North America and Europe (Fig. 2b,d) and across Patagonia and the Antarctic coast (Fig. 2a,c). In several regions, the sign of the association reverses between the winter and summer seasons. For example, in the Southern Hemisphere, a negative association over the larger parts of the Atacama region, southern Africa, and Australia in austral summer (Fig. 2a,c) changes to a positive association in austral winter (Fig. 2b,d), showing that wave breaking contributes to precipitation formation in these regions primarily during winter.

Relevance of RWB for precipitation increases with land aridity

The analysis above shows that RWB contributes to much of the precipitation equatorward and downstream of the midlatitude storm tracks where most of the world's arid regions are situated. In a next step, we link the relevance of RWB for precipitation to land with different degrees of aridity (see Methods). Much of the arid land, here defined by a semi-arid to hyper-arid climate, features a

significant positive association between precipitation and wave breaking, specifically across their poleward and westward flanks (Fig. 3a and Extended Data Fig. 8). In contrast, the equatorward and eastward flanks of these arid regions show to a varying extent a significant negative association, most prevalent over central Asia, the Atacama region, southern Africa, and Australia. This diagonally oriented dipole pattern over several prominent arid regions shows that the extratropical forcing through RWB into low latitudes is a key driver of precipitation in the poleward-westward portions of arid regions and suggests that tropical weather systems control much of the precipitation in the equatorward-eastward parts of arid regions.

Portions of land surface where precipitation has a positive association with RWB (see Methods) increase with land aridity. Across the four evaluated precipitation datasets, fractions of land surface where extreme precipitation occurrences have a positive association with RWB reach from 17-41% in world's humid regions up to 64-79% in regions with a hyper-arid climate (Fig. 3b). Similarly, land surface fractions where total annual precipitation amounts have a positive association with RWB increase from 24-54% in humid regions up to 71-83% in hyper-arid regions (Fig. 3c).

The increasing relevance of RWB for precipitation with land aridity is further examined using an estimate by how much precipitation is enhanced or reduced due to RWB, referred to as precipitation surplus (see Methods and Extended Data Fig. 9). Spatially aggregated precipitation surplus due to RWB ranges from 2% to a deficit of 7% in humid regions to a surplus of 7-14% in hyper-arid regions for extreme precipitation occurrences (Fig. 3b), and likewise, from a surplus of 1% to a deficit of 5% in humid regions to a surplus of 5-13% in hyper-arid regions for total precipitation amounts (Fig. 3c). Thus, from a spatially aggregated and year-round perspective, RWB tends to suppress precipitation in humid regions and enhances precipitation in arid regions. While the relatively low values can be expected given the strong regionally and seasonally varying relationship between precipitation and RWB, this analysis shows that also wave breaking contributions to precipitation increase with increasing land aridity.

A regional and seasonal perspective

To further understand the regionally and seasonally varying relevance of RWB for precipitation formation in arid regions, we further explore their relationship in eight prominent arid regions during traditionally defined seasons. These regions are (1) southwest North America, (2) central North America, (3) the southern Mediterranean, North Africa, and the Middle East, (4) central Asia, (5) the Atacama, (6) Patagonia, (7) southern Africa, and (8) Australia (Fig. 3a). Figure 4 shows the spatially

aggregated precipitation characteristics attributed to RWB in the same manner as in Fig. 3b,c, but based on seasonally partitioned precipitation over the arid portions of these eight regions only.

In subtropical arid regions (southwest North America, the Mediterranean - North Africa - Middle East, the Atacama, southern Africa, and Australia), RWB contributes to much of the precipitation during the transition seasons and winter (Fig. 4). In many of these regions and seasons, RWB substantially enhances precipitation, apart from Australia in MAM. Moreover, fractions of land surface where precipitation has a positive association with RWB reach from 40% to nearly 100%, showing that RWB widely governs precipitation formation in the arid subtropics during the transition seasons and winter, whether being the wetter (Mediterranean-North Africa-Middle East; Fig. 4c,k) or the drier (the Atacama, southern Africa, and Australia; Fig. 4e,g,h,m,o,p) seasons of the year. In contrast, during summer, precipitation has a systematic negative association with wave breaking in 40-100% of arid land surface, except for the Mediterranean-North Africa-Middle East region, and spatially aggregated precipitation surplus due to RWB show values of -5 to -19% over southwest North America, southern Africa and Australia (Fig. 4). Among these regions, southern Africa and Australia receive most of their precipitation during summer (Fig. 4g,h,o,p), consistent with the significant negative association across many of these regions in the year-round analysis (Fig. 3 and Extended Data Fig. 8). These findings demonstrate that arid subtropical regions receive much of their precipitation during the transition seasons and winter under the influence of extratropical forcing by breaking Rossby waves into low latitudes and suggest that tropical weather systems control much of the precipitation in these regions during the warm season when the tropical circulation exerts its most poleward influence.

Arid regions at extratropical latitudes receive precipitation under the influence of RWB during varying seasons throughout the year (Fig. 4). Central North America and Patagonia receive enhanced precipitation due to RWB during the transition seasons and summer, while precipitation is suppressed by RWB over central North America during winter. Over Central Asia, spatially aggregated precipitation surplus ranges from a weak deficit to moderate surplus, while the spatial patterns of precipitation surplus and deficit remain constant during the seasons (Supplement Figs. 2-5), suggesting that the influences of the extratropical and tropical circulation patterns on precipitation formation remain similar throughout the year. Thus, extratropical arid regions differ from their subtropical counterparts, as breaking Rossby waves govern precipitation formation in extratropical arid regions during varying seasons throughout the year, while this is confined to the transition seasons and winter for subtropical arid regions, consistent with the seasonality of the large-scale circulation.

Discussion

This study reveals that RWB is responsible for much of the precipitation in arid regions around the world. The importance of RWB for precipitation is particularly strong in the poleward and westward portions of subtropical arid regions, including those with a Mediterranean-type climate¹¹, where the extratropical forcing governs precipitation formation during the cool season through wave breaking into low latitudes. In contrast, the equatorward and eastward flanks of several prominent arid regions display a negative association between precipitation and RWB, suggesting that tropical weather systems regulate much of the precipitation generation during the warm season in these regions. Subtropical arid regions are typically situated at the transition between extratropical and tropical circulation regimes. As a result, these regions experience a strong seasonally alternating and geographically varying influence of both types of circulation regimes, making these regions likely very sensitive to climatic changes. In some regions, changes have been observed, or are projected to occur in the future, toward increased precipitation during the warm season⁵⁴ and reductions in cool season precipitation along with a ceasing of extratropical weather systems⁵⁵⁻⁵⁷.

The findings of this study have important societal and scientific implications for understanding and predicting extremes and climatic changes in the water cycle in arid regions around the world. Applying diagnostics of RWB to model forecasts has the potential to assist medium-range to subseasonal prediction of flood hazards in arid regions following the successful application of other weather system-based diagnostics to such forecasts with relevance to precipitation extremes in humid regions⁵⁸. Importantly, in the context of climate change, we note that wave breaking contributions to precipitation are particularly large in arid subtropical regions where climate models project a future decline in precipitation amounts¹⁶ and where projected changes in precipitation extremes suffer from large uncertainties¹⁷. This implies that the response of RWB to a warming climate is of direct relevance to the projected precipitation decline in these regions and that robust projections of future extreme precipitation changes critically depend on climate models' ability to accurately simulate this atmospheric process and associated precipitation generation. Extending our analysis to climate model simulations in future studies will thus help clarify the role of atmospheric dynamics in projections and uncertainties of future precipitation changes in societally vulnerable regions exposed to both flood hazards and freshwater shortages.

Literature

1. Feng, S. & Fu, Q. Expansion of global drylands under a warming climate. *Atmos. Chem. Phys.* **13**, 10081-10094 (2013).
2. Lickley, M. & Solomon S. Drivers, timing and some impacts of global aridity change, *Env. Res. Lett.* **13**, 104010 (2018).
3. Yin, J. Gao, Y., Chen, R., Yu, D., Wilby, R., Wright, N., Ge, Y., Bricker, J., Gong, H. & Guan M. Flash floods – why are more of them devastating the world’s driest regions? *Nature comments*, 615, 212-215 (2023).
4. Mirzabaev, A., Wu, J., Evans, J., García-Oliva, F., Hussein, I. A. G., Iqbal, M. M., Kimutai, J., Knowles, T., Meza, F., Nedjroaoui, D., Tena, F., Türkes, M., Vázquez, R. J., and Weltz, M. Desertification, in: *Climate Change and Land: an IPCC special report on climate change, desertification, land degradation, sustainable land management, food security, and greenhouse gas fluxes in terrestrial ecosystems*, edited by: Shukla, P. R., Skea, J., Buendia, E. C., Masson-Delmotte, V., Pörtner, H.-O., Roberts, D. C., Zhai, P., Slade, R., Connors, S., van Diemen, R., Ferrat, M., Haughey, S., Luz, S., Neogi, M., Pathak, M., Petzold, J., Portugal Pereira, J., Vyas, P., Huntley, E., Kissick, K., Belkacemi, M. & Malley, J. (2019).
5. Wang, L., Wenzhe, J., MacBean, N., Rulli, M. C., Manzoni, S., Vico, G. & D’Odorico, P. Dryland productivity under a changing climate. *Nat. Clim. Change.* **12**, 981-994 (2022).
6. Berdugo, M., Delgado-Baquerizo, M., Soliveres, S., Hernández-Clemente, R., Zhao, Y., Gaitán J. J., Gross, N. Saiz, H. Maire, V., Lehmann, A., Rillig, R. V., Solé, R. V. & Maestre, F. T. Global ecosystem thresholds driven by aridity, *Science*, **367**, 787-790 (2020).
7. Gleick, P. H. Water, drought, climate change, and conflict in Syria. *Weath. Clim. Soc.* **6**, 331-340 (2014).
8. Kelley, C. P., Mohtadi, S., Cane, M. A., Seager, R. & Kushnir Y. Climate change in the Fertile Crescent and implications of the recent Syrian drought. *Proc. Natl Acad. Sci.* **112**, 3241-3246 (2015).

9. Cattaneo, C., Beine, M., Fröhlich, C. J., Kniveton, D., Martinez-Zaroso, I., Mastrorillo, M., Millock, K., Piguet, E. & Schraven B. Human migration in the era of climate change, *Rev. Env. Econom. Policy*, **13**, 189-206 (2019).
10. He, J. & Soden, B. J. A re-examination of the projected subtropical precipitation decline. *Nat. Clim. Change* **7**, 53-57 (2017).
11. Seager, R., Osborn, T. J., Kushnir, Y., Simpson, I. R., Nakamura, J. & Liu, H. Climate variability and change of Mediterranean-Type climates. *J. Clim* **32**, 2887-2915 (2019).
12. Donat, M. G., Lowry, A. L., Alexander, L. V., O’Gorman, P. A. & Maher, N. More extreme precipitation in the world’s dry and wet regions. *Nat. Clim. Change* **6**, 508-513 (2016).
13. Donat, M. G., Angelil, O. & Ukkola, A. M. Intensification of precipitation extremes in the world’s humid and water-limited regions. *Env. Res. Lett.* **14**, 065003 (2019).
14. Zittis, G., Bruggeman, A. & Lelieveld, J. Revisiting future extreme precipitation trends in the Mediterranean. *Weath. Clim. Extremes* **34**, 100380 (2021).
15. Armon, M., Marra, F., Enzel, Y., Rostkier-Edelstein, D., Garfinkel, C. I., Adam, O., Dayan, U. & Morin, E. Reduced rainfall in future heavy precipitation events related to contracted rain area despite increased rain rate, *Earth’s Future*, **10**, e2021EF002397 (2022).
16. Shepherd, T. G. Atmospheric circulation as a source of uncertainty in climate change projections. *Nat. Geosci.* **7**, 703–708 (2014).
17. Pfahl, S., O’Gorman, P. A. & Fischer, E. M. Understanding the regional pattern of projected future changes in extreme precipitation. *Nat. Clim. Change* **7**, 423–427 (2017).
18. Pfahl, S. & Wernli, H. Quantifying the relevance of cyclones for precipitation extremes. *J. Clim.* **25**, 6770–6780 (2012).
19. Hawcroft, M., Shaffrey, L., Hodges, K. & Dacre, H. How much Northern Hemisphere precipitation is associated with extratropical cyclones? *Geophys. Res. Lett.* **39**, L24809 (2012).

20. Pfahl, S., Madonna, E., Boettcher, M., Joos, H. & Wernli, H. Warm conveyor belts in the ERA-Interim dataset (1979-2010). Part II: Moisture origin and relevance for precipitation. *J. Clim.* **27**, 27–40 (2014).
21. Catto, J. L., Jakob, C. & Nicholls, N. Relating global precipitation to atmospheric fronts. *Geophys. Res. Lett.* **39**, L10805 (2012).
22. Catto, J. L., Madonna, E., Joos, H., Rudeva, I. & Simmonds, I. Global relationship between fronts and warm conveyor belts and the impact on extreme precipitation. *J. Clim.* **28**, 8411–8429 (2015).
23. Waliser, D. & Guan, B. Extreme winds and precipitation during landfall of atmospheric rivers, *Nat. Geosci.* **10**, 179–183 (2017).
24. Guan, B. & Waliser, D. E. Detection of atmospheric rivers: Evaluation and application of an algorithm for global studies, *J. Geophys. Res. Atmos.* **120**, 12514–12535 (2015).
25. Khouakhi, A., Villarini, G. & Vecchi, G. A. Contribution of tropical cyclones to rainfall at the global scale, *J. Clim.* **30**, 359–372 (2017).
26. Hurley J. V. & Boos, W. R. A global climatology of monsoon low-pressure systems. *Q. J. Roy. Meteor. Soc.* **141**, 1049–1064 (2015).
27. Crétat, J., Vizy, E. K. & Cook, K.H.: The relationship between African easterly waves and daily rainfall over West Africa: observations and regional climate simulations, *Clim. Dynam.* **44**, 385–404 (2015).
28. Yang, L., Smith, J., Baeck, M. L., & Morin, E. Flash flooding in arid/semiarid regions: climatological analyses of flood-producing storms in central Arizona during the North American monsoon. *J. Hydrometeorol.* **20**, 1449–11471, (2019).
29. Sierks, M. D., Kalansky, J., Cannon, F., and Ralph, F. M. Characteristics, origins and impacts of summertime extreme precipitation in the Lake Mead Watershed. *J. Clim.* **33**, 2663–2680 (2020).

30. Armon, M., Dente, E., Smith, J. A., Enzel, Y. & Morin, E. Synoptic-scale control over modern rainfall and flood patterns in the Levant drylands with implications for past climates. *J. Hydrometeorol.* **19**, 1077-1096 (2018).
31. Ning, G., Luo, M., Zhang, Q., Wang, S., Liu, Z., Yang, Y., Wu, S. & Zeng Z. Understanding the mechanisms of summer extreme precipitation events in Zinjiang or arid northwest China, *J. Geophys. Res. Atm.* **126**, e2020JD034111 (2021).
32. Reyers, M., Boehm, C., Knarr, L., Shao, Y., Crewell, S. Synoptic-to-regional-scale analysis of rainfall in the Atacama Desert (18°-26°S) using a long-term simulation with WRF. *Mon. Weath. Rev.* **149**, 91-112 (2021).
33. Rapolaki, R. S., Blamey, R. C., Hermes, J. C. & Reason, C. J. C. A classification of synoptic weather patterns linked to extreme rainfall over the Limpopo River basin in southern Africa, *Clim Dynam.* **53**, 2265-2279 (2019).
34. Black, A. S. et al. Australian northwest cloudbands and their relationship to atmospheric rivers and precipitation. *Mon. Weath. Rev.* **149**, 1125-1139 (2021).
35. Knippertz, P. Tropical–extratropical interactions related to upper-level troughs at low latitudes, *Dynam. Atmos. Oceans* **43**, 36–62 (2007).
36. Ward, N., Fink, A. H., Keane, R. J. & Parker, D. J. Upper-level midlatitude troughs in boreal winter have an amplified low-latitude linkage over Africa, *Atmos. Sci. Lett.* **24**, e1129 (2022).
37. Abatzoglou, J. T. Contribution of cutoff lows to precipitation across the United States. *J. Appl. Meteorol. Clim.* **55**, 893–899 (2016).
38. Barbero, R., Abatzoglou, J. T. & Fowler, H. J. Contribution of large-scale midlatitude disturbances to hourly precipitation extremes in the United States, *Clim. Dynam.* **52**, 197–208 (2019).
39. Favre, A., Hewitson, B., Lennard, C., Cerezo-Mota, R. & Tadross, M. Cutoff lows in the South Africa region and their contribution to precipitation, *Clim. Dynam.* **41**, 2331–2351 (2013).

40. Grosfeld, N. H., McGregor, S. & Tschetto, A. S. An automated climatology of cool-season cutoff lows over southeastern Australia and relationships with the remote climate drivers. *Mon. Weath. Rev.* **149**, 4167-4181 (2021).
41. Wirth, V., Riemer, M., Chang, E. K. M. & Martius O. Rossby wave packets on the midlatitude waveguide – a review. *Mon. Weath. Rev.* **146**, 1965-2001 (2018).
42. White, R. H., Kornhuber, K., Martius, O. & Wirth, V. From atmospheric waves to heatwaves: A waveguide perspective for understanding and predicting concurrent, persistent, and extreme extratropical weather. *B. Am. Meteorol. Soc.* **103**, 923-935 (2022).
43. Screen, J. A. & Simmonds, I. Amplified mid-latitude planetary waves favour particular regional weather extremes, *Nat. Clim. Change* **4**, 704-709 (2014).
44. McIntyre, M. E. & Palmer, T. N. Breaking planetary waves in the stratosphere, *Nature* **305**, 593-600 (1983).
45. Appenzeller, C. & Davies, H. C. Structure of stratospheric intrusions into the troposphere, *Nature* **358**, 570–572 (1992).
46. Funatsu, B. M. & Waugh, D. W. Connections between potential vorticity intrusions and convection in the Eastern Tropical Pacific, *J. Atmos. Sci.* **65**, 987–1002 (2008).
47. Schlemmer, L., Martius, O., Sprenger, M., Schwierz, C. & Twitchett, A. Disentangling the forcing mechanisms of a heavy precipitation event along the alpine south side using potential vorticity inversion, *Mon. Weath. Rev.* **138**, 2336–2353 (2010).
48. Moore, B. J., Keyser, D. & Bosart, L. F. Linkages between extreme precipitation events in the central and eastern United States and Rossby wave breaking, *Mon. Weath. Rev.* **147**, 3327-3349 (2019).
49. Martius, O., Zenklusen, E., Schwierz, C. & Davies, H. C. Episodes of alpine heavy precipitation with an overlying elongated stratospheric intrusion: a climatology, *Int. J. Climatol.* **26**, 1149–1164 (2006).

50. De Vries, A. J., Ouwersloot, H. G., Feldstein, S. B., Riemer, M., El Kenawy, A. M., McCabe, M. F. & Lelieveld, J. Identification of tropical-extratropical interactions and extreme precipitation events in the Middle East based on potential vorticity and moisture transport, *J. Geophys. Res. Atmos.* **123**, 861-881 (2018).
51. Portmann, R. The life cycles of potential vorticity cutoffs: climatology, predictability, and high impact weather, PhD thesis, ETH Zurich (2020).
52. De Vries, A. J. A global climatological perspective on the importance of Rossby wave breaking and intense moisture transport for extreme precipitation events, *Weath. Clim. Dynam.* **2**, 129-161 (2021).
53. Shaw, T. A., Baldwin, M., Barnes, E. A., Caballero, R., Garfinkel, C. I., Hwang, Y.-T, Li, C., O’Gorman, P. A., Rivière G., Simpson, E. R. & Voigt, A. Storm track processes and the opposing influences of climate change, *Nature Geosci.* **9**, 656-664 (2016).
54. Raut, B. A., Jakob, C., & Reeder, M. J. Rainfall changes over southwestern Australia and their relationship to the Southern Annual Mode and ENSO. *J. Clim.* **27**, 5801-5814 (2014).
55. Pepler, A. S. & Rudeva, I. Anomalous subtropical zonal winds drive decreases in southern Australian frontal rain, *Weath. Clim. Dynam.* **4**, 175-188 (2023).
56. Zappa, G., Hawcroft, M. K., Shaffrey, L., Black, E. & Brayshaw, D. J. Extratropical cyclones and the projected decline of winter Mediterranean precipitation in the CMIP5 models. *Clim. Dynam.* **45**, 1727-1738 (2015).
57. Seager, R. & Vecchi, G. A. Greenhouse warming and the 21st century hydroclimate of southwestern North America, *Proc. Natl Acad. Sci.* **107**, 21277-21282 (2010).
58. DeFlorio, M. J., Waliser, D. E., Ralph, F. M., Guan, B., Goodman, A., Gibson, P. B., Asharaf, S., Monache, L. D., Zhang, Z. Subramanian, A. C., Vitart, C., Lin, H., and Kumar, A. Experimental Subseasonal-to-Seasonal (S2S) Forecasting of atmospheric rivers over the western United States, *J. Geophys. Res. Atmos.* **124**, 11242-11265 (2019).

Methods

Precipitation. Precipitation is a challenging meteorological variable to measure due to its very high spatiotemporal variability, specifically in arid regions⁵⁹. To obtain well-informed estimates of precipitation attributed to RWB, we use 4 precipitation products based on 3 different types of data sources: (1) the ERA5 reanalysis⁶⁰ of the European Centre for Medium-Range Weather Forecasts for 1979-2021, (2) the Integrated Multi-satellitE Retrievals of the Global Precipitation Measurement (GPM) Mission (IMERG)⁶¹, final version 6, for 2001-2020, (3) the Climate Prediction Center (CPC) global unified gauge-based analysis of daily precipitation⁶² of the National Oceanic and Atmospheric Administration (NOAA) for 1979-2021, and (4) the Multi-Source Weighted-Ensemble Precipitation (MSWEP)⁶³ version V280 for 1979-2020. Each of these data sources has its own strengths and limitations⁶⁴. Precipitation from reanalysis has a full coverage across space and time, and is generated by a physically consistent model, but stems from a short-range model forecast at a relatively coarse resolution and relies on parameterization for convective precipitation. The GPM IMERG product has a very high spatiotemporal resolution and provides measurements for regions with limited station density, but has deteriorated accuracy over mountains⁶⁵ and arid regions^{65,66}, reduced coverage toward higher latitudes⁶⁶, and covers only the period since 2000. CPC precipitation is directly derived from ground-based observations, but rain gauge observations are subject to measurement errors, interrupted time series, and limited station density, particularly in arid regions⁶⁷. The MSWEP product is based on the combination of these three different data sources to leverage their respective strengths⁶³. Daily precipitation fields from each dataset are interpolated using first-order conservative remapping on a 0.5-degree regular grid to facilitate the attribution to RWB at the grid scale. Extreme precipitation days are defined by daily precipitation amounts that exceed the 99th percentile of all days throughout the period under consideration (Supplement Fig. 1). For the seasonal analysis, we use the same selection of year-round defined extreme precipitation days and partition these across the corresponding seasons.

Identification of RWB. Data are retrieved from the ERA5 reanalysis on a global 0.5-degree regular grid at 6-h time intervals. Potential vorticity (PV) is computed from data on model levels and then interpolated onto isentropic surfaces between 275-360K with 5K intervals. PV fields are smoothed using a 9-point local smoothing to reduce excessive small-scale PV structures. For the detection of RWB we combine the object-based identification methods of PV streamers and cutoffs (Extended Data Fig. 2), first introduced by ref 68, and using some of the newer adaptations from refs 50,52,69 for PV streamers, and from refs 70,71 for PV cutoffs. Other studies have used other indicators of RWB, such as PV contour advection⁷², meridional reversal of PV⁷³, and meridionally overturning contours of

PV^{74,75}, potential temperature⁷⁶, or absolute vorticity⁷⁷. Here we briefly summarize the applied identification method in this study and refer for more details, motivations for specific choices, and sensitivity analyses to refs 50,52,68-71.

The detection of PV streamers and cutoffs is based on PV fields on single isentropic surfaces and follows three steps. First, we define in each hemisphere the stratospheric reservoir by the +2 potential vorticity unit (PVU; $1 \text{ PVU} = 10^{-6} \text{ kg K}^{-1} \text{ m}^2 \text{ s}^{-1}$) contour (-2 PVU contour in the Southern Hemisphere) - representing the dynamical tropopause - at the lowest latitude that encircles the Pole. If no circumglobal PV contour is present, the longest +/-2 PVU contour is designated as the stratospheric reservoir, provided it spans more than 180° in the zonal direction and reaches at least partly poleward of +/- 80° N. Assigned stratospheric reservoirs are evaluated on their vertical connection up to the 360K isentropic surface to avoid erroneous classification of large-scale high PV air masses near the Earth's surface over the Poles as stratospheric reservoir. Additionally, stratospheric reservoirs that intersect with the Earth's surface as a result of the interpolation of PV fields from model levels to isentropic surfaces are removed.

Second, PV streamers are defined by elongated structures in the +/-2 PVU contours that encircle the stratospheric reservoir. Each combination of contour points (A and B), obtained by the *get_isolines* function of NCL version 6.6.2, on the +/-2 PVU contour is evaluated on the four following geometric criteria (see also ref 52, their Fig. 1): (1) the width (the great-circle distance between points A and B) $< 1,500 \text{ km}$, (2) the length (the largest great circle distance of any contour point between points A and B, and the great circle of points A and B) $> 1,000 \text{ km}$, (3) the ratio length over width > 1 , after refs 50,52, and (4) the length along the contour between points A and B $< 15,000 \text{ km}$, after ref 69. If more than 50% of the stratospheric reservoirs' surface is classified as streamer, all streamers are removed on that isentropic surface.

Third, all remaining $> 2 \text{ PVU}$ ($< -2 \text{ PVU}$ in the Southern Hemisphere) air masses that are not part of the stratospheric reservoir are considered as potential PV cutoffs. PV cutoffs are scrutinized on their vertical connection to the stratospheric reservoir aloft and low moisture content (specific humidity $< 0.1 \text{ g kg}^{-1}$ and relative humidity $< 70\%$ for at least 50% of the PV cutoff surface area) to remove PV structures with an orographic frictional and diabatic origin, respectively, after refs 70,71. Only PV cutoffs with a surface area $< 5 \times 10^6 \text{ km}^2$, after ref 71, and $> 2.5 \times 10^4 \text{ km}^2$ are retained to focus on synoptic-scale structures.

Attribution of precipitation to RWB. Precipitation forming under the influence of wave breaking typically occurs at the downstream flank of the breaking waves (see Extended Data Fig. 1). The upper-level forcing and associated cyclonic circulation of the breaking waves induces poleward moisture transport and dynamical lifting at this location^{46,47,49,52}. Therefore, to attribute precipitation to wave breaking, we provide the PV structures with an extended area around their circumference using a fixed distance of 500 km, adjusted from refs 51,52. Precipitation is attributed to wave breaking based on the following spatiotemporal criteria. Daily precipitation extremes as well as daily precipitation amounts are attributed to RWB if PV structures, including their extended area, overlap with precipitation at the grid scale on at least 3 of the 5 time intervals during daily precipitation (00, 06, 12, and 18 UTC of the same day and 00 UTC of the next day) on at least 2 isentropic surfaces as a proxy of wave breaking with a vertical depth of approximately 10K or more. Extended Data Figure 1 demonstrates the attribution of extreme precipitation to PV structures based on eight extreme precipitation events in different arid parts of the world.

Positive and negative associations and statistical significance testing. To examine the relationship between precipitation and RWB, we determine where this relationship has a positive or negative association and where this association can be considered significant. To this end, we follow the following procedure, which includes the testing of the null hypothesis that precipitation and RWB occur independently, and this hypothesis is rejected in regions where precipitation co-occurs with RWB significantly more or less than expected under independence (i.e., a two-sided test).

First, we perform a Monte Carlo test whereby the dates of PV streamers and cutoffs are shuffled by taking a random day in the same month of a different year, while the dates of precipitation are kept as in reality. In this way, the seasonal influence on the relationship between precipitation and wave breaking is accounted for. This procedure is repeated 100 times for the entire period under consideration. At each grid cell, the Monte Carlo test results in 100 computed fractions of precipitation attributed to wave breaking assuming an independent relationship. The *p*-value is then determined based on the ranking of the observed fraction of precipitation attributed to RWB as in reality within the distribution of 100 fractions based on random matching.

Second, we control the number of false rejections of the null hypothesis by using the false discovery rate (FDR) test⁷⁸ with $\alpha = 0.1$. Grid points with > 50% missing values are not included in the FDR test. This procedure yields global fields with information at each grid point indicating whether the relationship between precipitation and RWB has a *significant positive*, *nonsignificant*, or *significant*

negative association. A significant positive association indicates that precipitation is significantly more likely to occur in the presence of RWB than under climatology (i.e., normal conditions). A significant negative association indicates that precipitation is significantly less likely to occur in the presence of wave breaking than under climatology, suggesting the dominance of other weather systems for precipitation generation that tend to *not* co-occur with wave breaking. This procedure is repeated for both precipitation extremes and total amounts, for the year-round and seasonal analyses, and for each precipitation dataset.

The results from the significance testing inherently depend on the sample size, i.e., the length of the datasets that differ among the used precipitation products. To obtain consistent indications of spatially aggregated land surface where RWB favors precipitation formation, we define in addition to the significant associations, also nonsignificant positive and negative associations between precipitation and RWB at grid points where the observed fraction is larger and smaller, respectively, than the median of the fractions from the Monte Carlo samples. While positive and negative associations do not indicate statistical significance, the sign of the association is much less dependent on the length of the respective data records and is thus more easily compared across datasets with different lengths.

Precipitation surplus. Precipitation fractions associated with RWB can be large even in regions where there is a significant negative association between precipitation and RWB, for example, in much of the humid extratropics, where wave breaking occurs relatively frequently. To obtain estimates by how much precipitation is enhanced or reduced due to RWB (note the difference to “precipitation associated with RWB”), we introduce a measure termed the precipitation surplus, denoted S . First, we compute the daily precipitation rate conditional to days *without* RWB, R_{noRWB} , and derive the total precipitation that would have formed throughout the period under consideration assuming the absence of RWB, by multiplying R_{noRWB} by the number of days in the considered time period (i.e., the length of the respective precipitation datasets, days with missing values excluded), yielding P_{noRWB} . The difference between the observed total precipitation, denoted P , and total precipitation in absence of RWB yields the so-called precipitation surplus, i.e., $S = P - P_{noRWB}$. We compute the precipitation surplus S for all months separately to account for the seasonality in the relationship between precipitation and RWB and then sum it across the year or seasons, corresponding to the respective analyses in this study. Fractions of precipitation surplus are expressed relative to total precipitation at the grid scale (Extended Data Fig. 9 and Supplement Figs. 2-5) or based on spatially aggregated quantities (Figs. 3b,c and 4). Spatial aggregations of precipitation surplus are area-weighted based on

the surface area that each grid point represents. Identical computations are performed for both the *extreme precipitation occurrences* and *precipitation amounts*. This approach provides an ad hoc estimate of the precipitation that forms due to (surplus) or is suppressed by (deficit) RWB and supports an adequate comparison of RWB contributions to precipitation across regions with a spatially varying RWB climatology.

Differences in results from the varying precipitation datasets. All analyses in this study, from global to regional scales and from year-round to seasons, show generally robust results across the four evaluated precipitation datasets, providing confidence in the results. However, we note a systematic lower contribution of RWB to precipitation based on GPM IMERG compared to the other three datasets (ERA5, CPC, and MSWEP) in terms of local associations (Figs. 1 and 2, Extended Data Figs. 4-7), spatially aggregated land surface with a positive association (Figs. 3b,c and 4) and spatially aggregated precipitation surplus (Figs. 3b,c and 4), particularly in midlatitudes during winter (Fig. 4). Although well beyond the scope of this paper to investigate this further, we speculate that these differences may directly stem from the abovementioned strengths and limitations of satellite-based measurements. Local convective precipitation, for which synoptic-scale processes such as RWB can be of reduced relevance compared to large-scale precipitation, may be better represented in GPM IMERG than in the relatively coarse resolution precipitation forecasts from reanalysis, while these storms may be missed by stations due to the low-density network in arid regions. On the other hand, precipitation from GPM IMERG has reduced accuracy over mountains and arid regions^{65,66}, and for winter precipitation and snowfall^{65,66}, which may contribute to the differences between the datasets, particularly the large differences for winter precipitation in the midlatitudes (Fig. 4).

Eddy kinetic energy. To illustrate the location and intensity of the midlatitude storm tracks, we compute the eddy kinetic energy (EKE) using the 10-day high-pass filtered (fast Fourier transform) horizontal wind of ERA5 at a regular 2-degree grid at 6-h time steps and vertically integrate the mass-weighted EKE across 37 pressure levels between 1-1000 hPa, adjusted from ref 53.

Aridity index. We retrieved monthly precipitation and potential evapotranspiration from the Climate Research Unit (CRU) dataset⁷⁹ for the period 1979-2021. The data have a global coverage over land except for Antarctica. The aridity index (AI) is computed as the ratio of precipitation over potential evapotranspiration ($AI = \text{precipitation} / \text{potential evapotranspiration}$), and the AI categories are defined as follows, following refs 59,80: humid ($AI \geq 0.65$); dry-subhumid ($0.5 \leq AI < 0.65$); semi-arid ($0.2 \leq AI < 0.5$); arid ($0.05 \leq AI < 0.2$); and hyper-arid ($AI < 0.05$).

Data availability

All datasets used in this study are freely available from the respective data providers. ERA5 reanalysis data from the ECWMF were obtained via the MARS archive and are also available from the Climate Data Store (<https://cds.climate.copernicus.eu>). Other datasets used for precipitation were accessed from NASA (<https://gpm1.gesdisc.eosdis.nasa.gov>) for GPM-IMERG, from NOAA (<https://downloads.psl.noaa.gov>) for CPC, and from GloH2O (<https://www.gloh2o.org>) for MSWEP, while monthly data from CRU were obtained via <https://data.ceda.ac.uk/badc/cru/>. Societal impacts from 8 demonstrative extreme precipitation events driven by RWB were obtained from the Emergency event database (EM-DAT) via <https://www.emdat.be>, accessed on 24-10-2023.

References

59. Morin, E., Marra, F. & Armon M. Dryland precipitation climatology from satellite observations in Satellite precipitation measurements, *Advances in Global Change Research* 69 (Springer Nature Switzerland, 2020).
60. Hersbach, H. et al. The ERA5 global reanalysis. *Quart. J. Roy. Meteorol. Soc.* **146**, 1999-2049 (2020).
61. Huffman, G. J., Bolvin, T. D., Braithwaite, D., Hsu, K.-L. Joyce, R. J., Kidd, C., Nelkin, E. J., Sorooshian, S., Stocker, E. F., Tan, J., Wolff, D. B., & Zie, P. Integrated multi-satellite retrievals for the Global Precipitation Measurement (GPM) Mission (IMERG). *Adv. Glob. Change Res.*, **67**, 343-353, https://doi.org/10.1007/978-3-030-24568-9_19 (2020).
62. Chen, M., Shi, W., Xie, P., Silva, V. B. S. Kousky, V. E., Wayne Higgins, R. & Janowiak, J. E. Assessing objective techniques for gauge-based analyses of global daily precipitation. *J. Geophys. Res. Atmos.* **113**, D04110, doi:10.1029/2007JD009132 (2008).
63. Beck, H. E., Wood, E. F., Pan, M., Fisher, C. K., Miralles, D. G., Van Dijk, A. I. J. M., McVicar, T. R. & Adler, R. F. MSWEP V2 Global 3-hourly 0.1° precipitation, *B. Am. Meteorol. Soc.* **100**, 473-500 (2019).
64. Sun, Q., Miao, C., Duan, Q. Ashouri, H., Sorooshian, S. & Hsu, K.-L. A review of global precipitation data sets: Data sources, estimation, and intercomparison, *Rev. Geophys.* **56**, 79-107 (2018).

65. Pradhan, R. K. et al. Review of GPM IMERG performance: a global perspective, *Remote Sens. Env.* **268**, 112754 (2022).
66. Li, Z., Tang, G. Hong, Z., Chen., M., Gao, S., Kirstetter, P., Gourley, J. J., Wen, Y., Yami, T., Nabih, S. & Hong Y. Two-decades of GPM IMERG early and final run products intercomparison: similarity and difference in climatology, rates, and extremes, *J. Hydrol.* **594**, 125975 (2021).
67. Kidd, C., Becker, A., Huffman, G. J., Muller, C. L., Joe, P., Skofronick-Jackson, G. & Kirschbaum, D. B. So, how much of the Earth's surface is covered by rain gauges? *B. Am. Meteorol. Soc.* **98**, 69-78 (2017).
68. Wernli, H. & Sprenger, M. Identification and ERA-15 climatology of potential vorticity streamers and cutoffs near the extratropical tropopause, *J. Atmos. Sci.* **64**, 1569–1586 (2007).
69. Sprenger, M., Martius, O. & Arnold, J. Cold surge episodes over southeastern Brazil - a potential vorticity perspective, *Int. J. Climatol.* **33**, 2758-2767 (2013).
70. Skerlak, B., Sprenger, M., Pfahl, S., Tyrlis, E. & Wernli, H. Tropopause folds in ERA-Interim: Global climatology and relation to extreme weather events, *J. Geophys. Res. Atmos.* **120**, 4860-4877 (2015).
71. Portmann, R., Sprenger, M. & Wernli, H. The three-dimensional life cycles of potential vorticity cutoffs: a global and selected regional climatologies in ERA-Interim (1979-2018). *Weath. Clim. Dynam.* **2**, 507-534 (2021).
72. Scott, R. K. & Cammas J. -P. Wave breaking and mixing at the subtropical tropopause, *J. Atmos. Sci.* **59**, 2347-2361 (2002).
73. Postel, G. A. & Hitchman, M. H. A climatology of Rossby wave breaking along the subtropical tropopause, *J. Atmos. Sci.* **56**, 359-373 (1999).
74. Ndarana, T. & Waugh, D. W. A climatology of Rossby wave breaking on the Southern Hemisphere tropopause, *J. Atmos. Sci.* **68**, 798-811 (2011).

75. Strong, C. & Magnusdottir, G. Tropospheric Rossby wave breaking and the NAO/NAM, *J. Atmos. Sci.* **65**, 2861-2876 (2011).
76. Bowley, K. A., Gyakum, J. R. & Atallah E. H. A new perspective toward cataloging Northern Hemisphere Rossby wave breaking on the dynamic tropopause, *Mon. Weath. Rev.* **147**, 409-431 (2019).
77. Barnes, E. A. & Hartmann, D. L. Detection of Rossby wave breaking and its response to shifts of the midlatitude jet with climate change, *J. Geophys. Res. Atmos.* **117**, D09117 (2012).
78. Wilks, D. S. "The stippling shows statistically significant grid points": How research results are routinely overstated and overinterpreted, and what to do about it. *B. Am. Meteorol. Soc.* **97**, 2263-2273 (2016).
79. Haris, I., Osborn, T. J., Jones, P. & Lister, D. Version 4 of the CRU TS monthly high-resolution gridded multivariate climate datasets, *Sci. Data* **7**, 109 (2020).
80. Middleton, N. & Thomas, D. World Atlas of Desertification, United Nations Environment Programme, (Arnold publishers, John Wiley & Sons, Inc., 1997).

Author contributions

All authors contributed to the conceptualization of the study and M.R. conceived the concept of precipitation surplus. A.V. constructed the figures and wrote most of the manuscript. All authors contributed to the interpretation of the results and editing of the paper.

Extended Data Table 1. Societal impacts of 8 flood-related natural disasters in arid regions linked to RWB¹

No.	Date	Country	Location (provinces)	Deaths	Affected people	Damage USD (million)
1	24 Nov 2013	United States	Oklahoma, Texas, California, New Mexico, Arizona	14		2,513
2	4-8 May 2007	United States	Colorado, Iowa, Kansas, Minnesota, Missouri, Nebraska, Oklahoma, South Dakota	12	40	494,010
3	10-11 Sep 2023	Libya	Cyrenaica (Derna)	4,000 ²		
4	21-29 Jul 2002	China	Xinjiang, Uygur, Zizhiqu	11	12,312	62,802
5	19 Jun 1991	Chile	Antofagasta	141	82,811	12,893
6	5-21 Apr 2017	Argentina	Chubut	1	9,000	
7	25 Jul – 3 Aug 2016	South Africa	Western Cape, Kwazulu Natal	7	6,900	219,485
8	10-22 Sep 2016	Australia	Victoria, South Australia	1	280	30,484

¹⁾ The data are taken from the Emergency Event Database (EM-DAT), accessed on 24-10-2023, except for the flood in Libya.

²⁾ At the time of submission of this manuscript, this event is not yet reported in the EM-DAT. A BBC news article from 10 October 2023 reports that at least 4,000 people are confirmed dead and another 10,000 missing (<https://www.bbc.com/news/world-africa-66961312>).

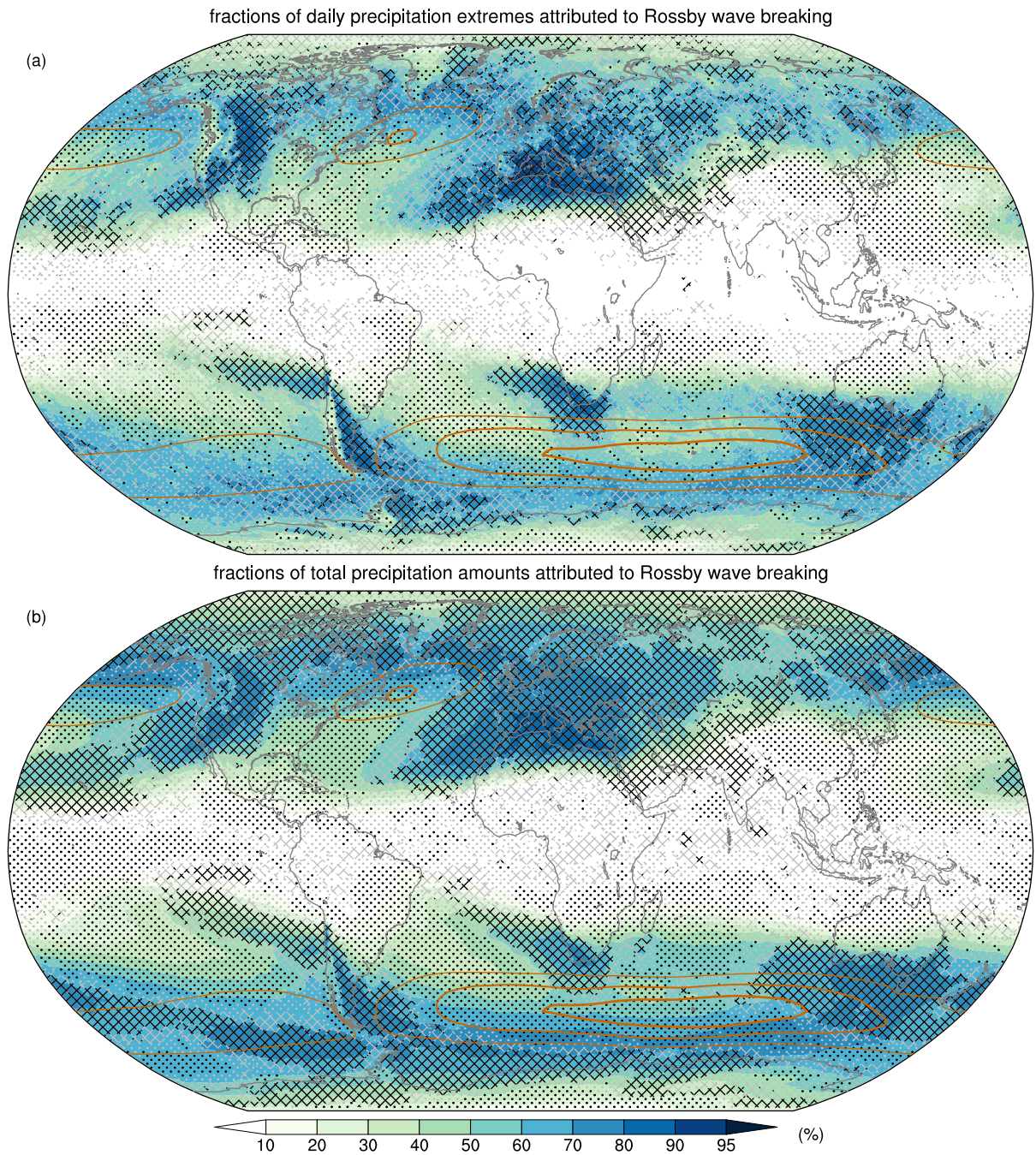


Figure 1. Contribution of RWB to year-round precipitation. Fractions of year-round ERA5 daily extreme precipitation occurrences (a) and total precipitation amounts (b) associated with RWB for 1979-2021. Crossed hatching and stippling in black (gray) indicate regions where the relationship between precipitation and RWB has a significant (nonsignificant) positive and negative association, respectively (see Methods). Orange contours denote the midlatitude storm tracks based on annual mean eddy kinetic energy (EKE; see Methods) at 0.7, 0.85, and 1. MJ m^{-2} intervals.

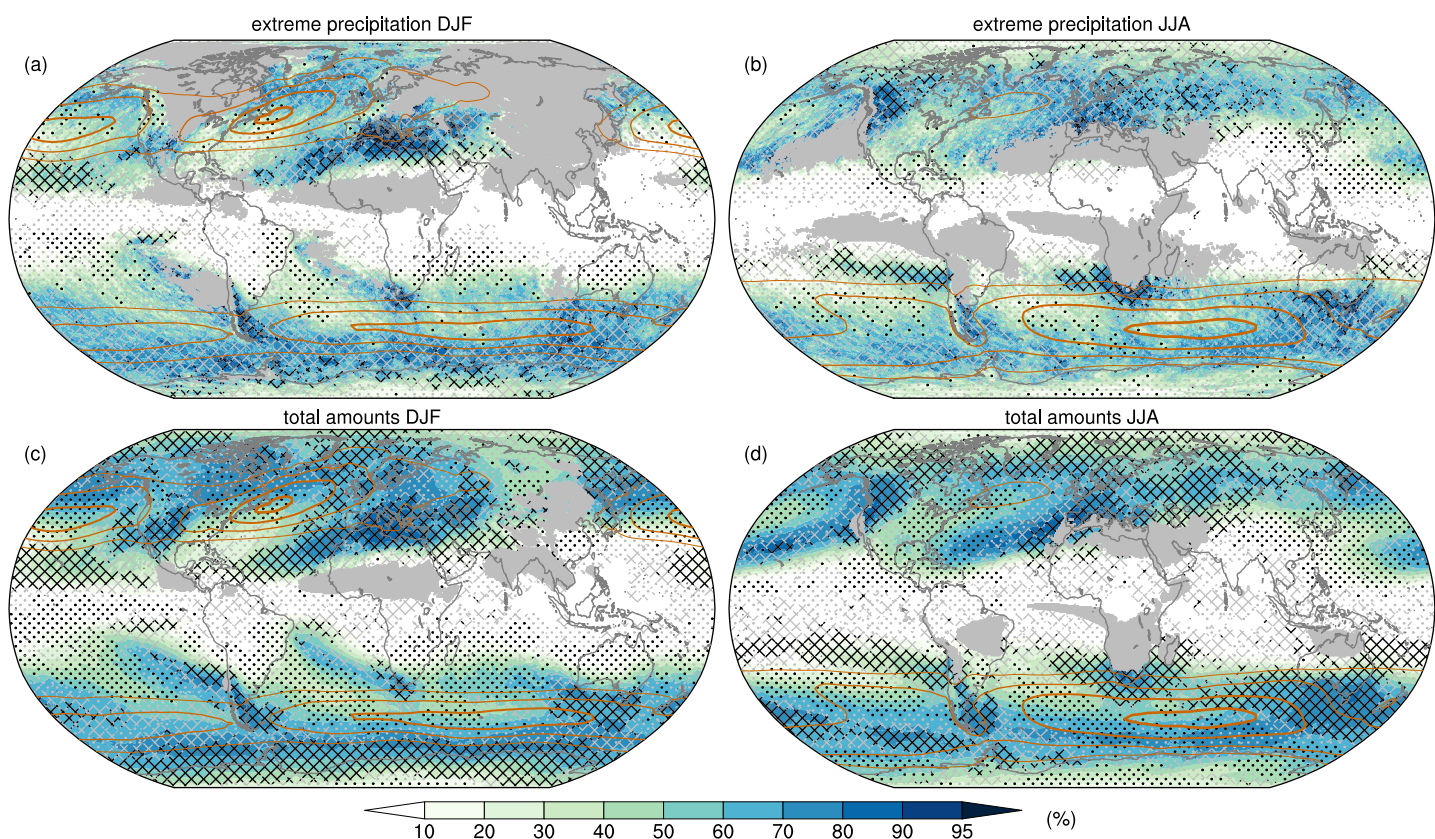


Figure 2. Contribution of RWB to seasonal precipitation. Fractions of ERA5 daily extreme precipitation occurrences (a,b) and total seasonal precipitation amounts (c,d) associated with RWB in DJF (a,c) and JJA (b,d). Regions where extreme precipitation occurrences (a,b) and seasonal amounts (c,d) fall below 5% of the year-round extreme precipitation occurrences and total amounts, respectively, are masked in gray. Crossed hatching and stippling in black and gray denote associations as in Fig. 1, but for the respective seasons. Orange contours denote the midlatitude storm tracks based on the corresponding seasonal mean EKE at 0.5, 0.7, 0.9, and 1.1 MJ m⁻² intervals.

Aridity Index and relationship between total annual precipitation amounts and Rossby wave breaking

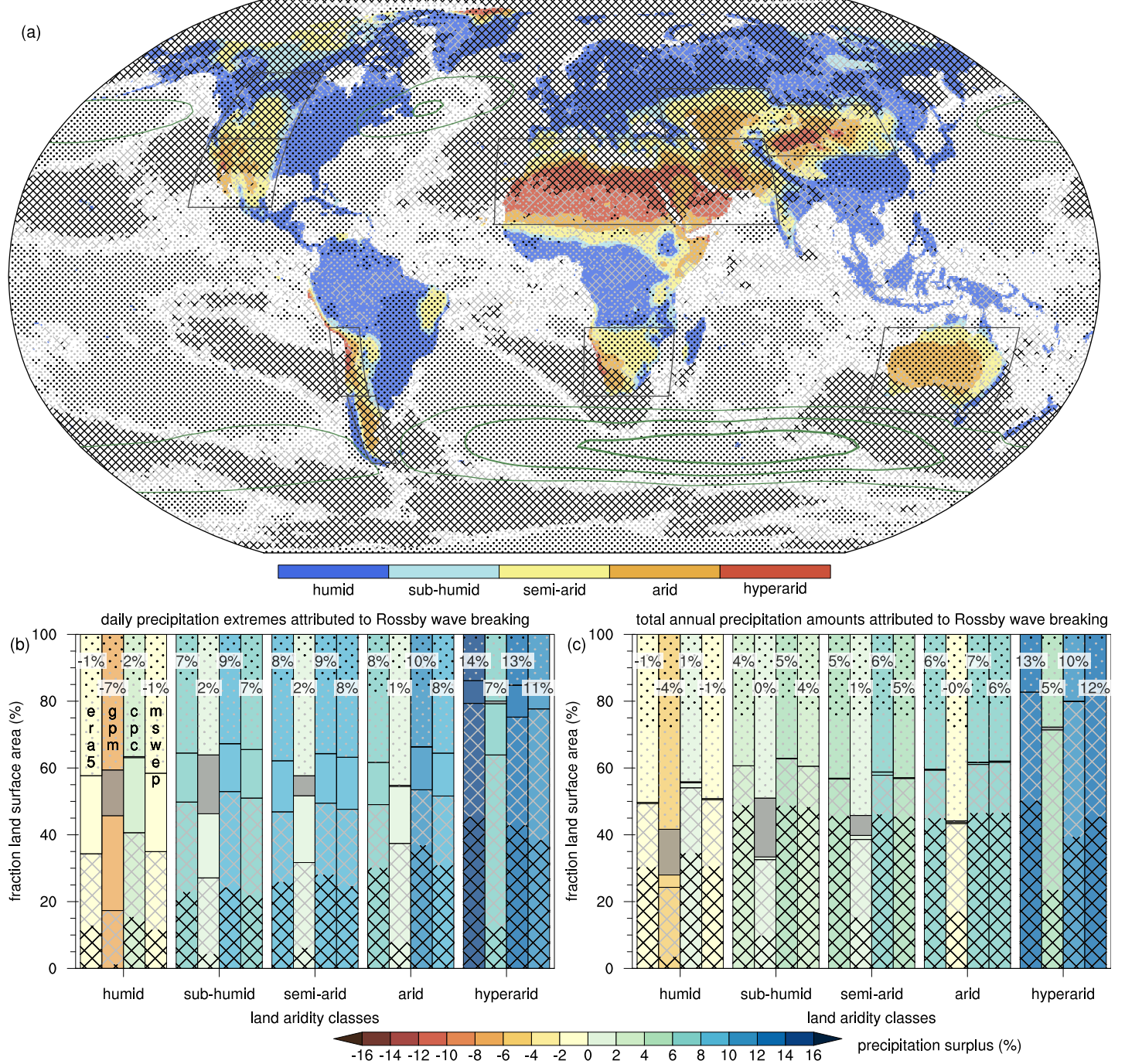


Figure 3. Relevance of RWB for precipitation in arid regions. a, Global aridity index categories, Antarctica excluded, and the associations between ERA5 total annual precipitation amounts and RWB in black and gray hatching and dots, as in Fig. 1b. Green contours denote the midlatitude storm tracks as in Fig. 1. b,c, bar segments represent fractions of land surface where precipitation has a positive (crossed hatching) or negative (stipples) association with RWB, considered significant in black and nonsignificant in gray, for the five aridity index categories for extreme precipitation occurrences (b) and total precipitation amounts (c). Gray shaded parts of the bar denote the fraction of land surface where precipitation datasets have missing values for > 50% of all days. The colors and numbers in b,c indicate the spatially aggregated precipitation surplus due to RWB (see Methods) as a fraction of the total precipitation over land from the different aridity index categories based on precipitation from, left to right, ERA5, GPM IMERG, CPC, and MSWEP.

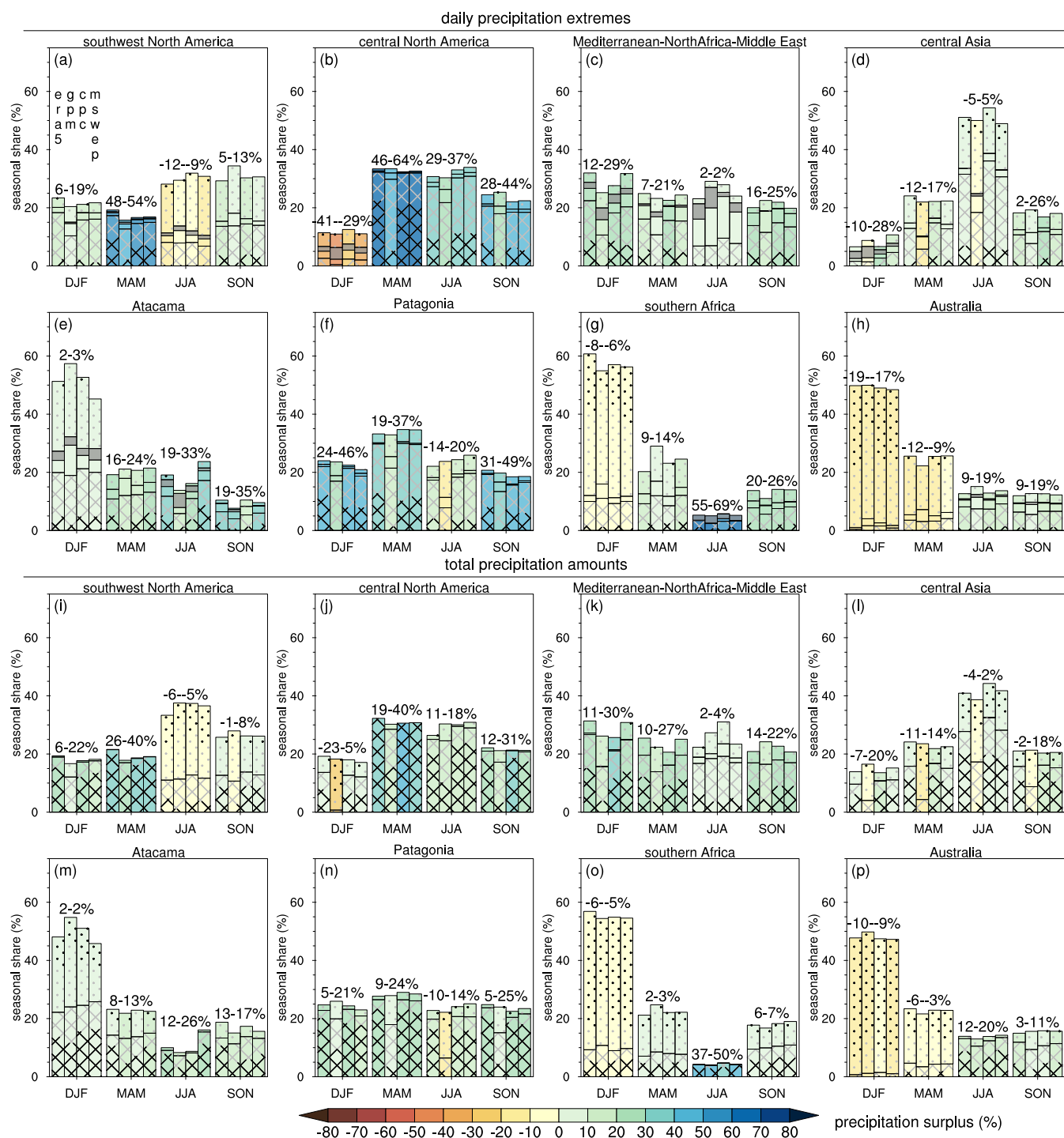


Figure 4. Contribution of RWB to precipitation in selected arid regions and seasons. Seasonal distribution of extreme precipitation occurrences (a-h) and total precipitation amounts (i-p) in eight selected arid regions, indicated by the gray boxes in Fig. 3a, considering their portions with a semi-arid to hyper-arid climate only: southwest North America; 123-95 W, 20-40 N (a,f), central North America; 123-95 W, 40-60 N (b,j), the southern Mediterranean, North Africa, and the Middle East; 20 W-75 E, 15-40 N (c,k), central Asia; 40-85 E, 40-55 N and 75-120 E, 35-50 N (d,l), the Atacama region; 75-65 W, 15-35 S (e,m), Patagonia; 72.5-62.5 W, 35-55 S (f,n), southern Africa; 10-40 E, 15-35 S (g,o), and Australia; 110-155 W, 15-40 S (h,p). The bar height denotes the fraction of the seasonal precipitation from the annual total, and the bar segments with crossed hatching and stipples reflect the fraction of arid land surface where the relationship between precipitation and RWB has a positive or negative association, respectively, significant in black and nonsignificant in gray. Gray shaded parts of the bar denote the fraction of land surface without any precipitation during that season or where the precipitation dataset has > 50% missing values for all days during that season. The color in the bars indicate the spatially aggregated precipitation surplus due to RWB as a fraction of the seasonal precipitation in these regions based on precipitation from, left to right, ERA5, GPM IMERG, CPC, and MSWEP, while the numbers above the bars show the corresponding minima and maxima across the four evaluated precipitation datasets.